Theory of Midinfrared Absorption Microspectroscopy: I. Homogeneous Samples

Brynmor J. Davis,[†] P. Scott Carney,[‡] and Rohit Bhargava*,[†]

Department of Bioengineering, Department of Electrical and Computer Engineering, and the Beckman Institute for Advanced Science and Technology, University of Illinois at Urbana–Champaign, Urbana, Illinois 61801

Midinfrared (IR) microspectroscopy is widely employed for spatially localized spectral analyses. A comprehensive theoretical model for the technique, however, has not been previously proposed. In this paper, rigorous theory is presented for IR absorption microspectroscopy by using Maxwell's equations to model beam propagation. Focusing effects, material dispersion, and the geometry of the sample are accounted to predict spectral response for homogeneous samples. Predictions are validated experimentally using Fourier transform IR (FT-IR) microspectroscopic examination of a photoresist. The results emphasize that meaningful interpretation of IR microspectroscopic data must involve an understanding of the coupled optical effects associated with the sample, substrate properties, and microscopy configuration. Simulations provide guidance for developing experimental methods and future instrument design by quantifying distortions in the recorded data. Distortions are especially severe for transflection mode and for samples mounted on certain substrates. Last, the model generalizes to rigorously consider the effects of focusing. While spectral analyses range from examining gross spectral features to assessing subtle features using advanced chemometrics, the limitations imposed by these effects in the data acquisition on the information available are less clear. The distorting effects are shown to be larger than noise levels seen in modern spectrometers. Hence, the model provides a framework to quantify spectral distortions that may limit the accuracy of information or present confounding effects in microspectroscopy.

Infrared (IR) absorption spectroscopy has been coupled to microscopy in various configurations for over 50 years.[1] The modern coupling of an interferometer with a microscope and mapping stage has enabled raster recording of Fourier transform infrared (FT-IR) spectra,[2] considerably accelerating the numbers of studies and scope of analysis by making instrumentation practical.[3] Numerous applications have been reported, for example, in materials science,[4] forensics,[5] and biomedical research.[6,7] For a number of reasons, these raster mapping systems are best utilized for point examination of specific sample areas.[8] Significantly higher imaging speeds and practical wide-field imaging can now be routinely attained by FT-IR microspectroscopy with focal plane array (FPA) detectors.[9,10] Hence, one can consider the current state of mid-IR microscopy to consist of two diverging modes. In the first, point microspectroscopy is conducted on small, homogeneous domains. The data acquisition is often guided by visible-band microscopy that is parfocal and colinear with the IR beam in the instrument; this mode is called point microscopy. The second major modality utilizes array detectors to measure across large areas of samples, with a spectrum recorded for each of tens to thousands of pixels; this mode is called imaging. The two modes are related and collectively termed microspectrosopy, in that both use focusing to collect spectra from small regions.

Ideally, FT-IR microspectroscopy can be thought to be an extension of IR spectroscopy localized to specific points in the sample. However, as FT-IR microspectroscopy is currently practiced,[3] this description is not accurate. The geometry of the sample boundaries, the morphology within the sample, the surrounding media, and the imaging optics all affect the measurements. In any given data set, the net contribution of all of these effects is observed, so that the spectra generally differ from the spectral response of the bulk material in the sample. Previous analyses of spectral differences between bulk and microscopy data have focused on the effects of stray light, the effects of oblique incidence on corrections to Beer's law[11] and orientation measurements.[4] Reports of optical distortions in FT-IR imaging have focused on the role of interfaces,[12] on scattering at an edge[13] and on scattering by the sample.[14] Distortions in a reflection–absorption (transflection)

---

(1) Norris, K. P. *J. Sci. Instrum.* **1954**, *31*, 284–287.

(2) Kwiatkoski, J. M.; Reffner, J. A. *Nature* **1987**, *328*, 837–838.

(3) *The Design, Sample Handling, and Applications of Infrared Microscopes*, ASTM STP 949; Roush, P. B., Ed.; American Society for Testing and Materials: West Conshohochen, PA, 1985.

(4) Koenig, J. L. *Spectroscopy of Polymers*, 2nd ed.; Elsevier: Amsterdam, The Netherlands, 1999.

(5) Bartick, E. G.; Tungol, M. W.; Reffner, J. A. *Anal. Chim. Acta* **1994**, *288*, 35–42.

(6) Wetzel, D. L.; LeVine, S. M. *Science* **1999**, *285*, 1224–1225.

(7) *Infrared and Raman Spectroscopy of Biological Materials*; Gremlich, H.-U., Yan, B., Eds.; Practical Spectroscopy; Marcel Dekker: New York, 2000.

(8) Bhargava, R.; Wall, B. G.; Koenig, J. L. *Appl. Spectrosc.* **2000**, *54*, 470–479.

(9) Levin, I. W.; Bhargava, R. *Annu. Rev. Phys. Chem.* **2005**, *56*, 429–474.

(10) Lewis, E. N.; Treado, P. J.; Reeder, R. C.; Story, G. M.; Dowrey, A. E.; Marcott, C.; Levin, I. W. *Anal. Chem.* **1995**, *67*, 3377–3381.

(11) Blout, E. R.; Bird, G. R.; Grey, D. S. *J. Opt. Soc. Am.* **1950**, *40*, 304–313.

(12) Bhargava, R.; Wang, S.-Q.; Koenig, J. L. *Appl. Spectrosc.* **1998**, *52*, 323–328.

(13) Romeo, M.; Diem, M. *Vib. Spectrosc.* **2005**, *38*, 129–132.

(14) Lee, J.; Gazi, E.; Dwyer, J.; Brown, M. D.; Clarke, N. W.; Nicholson, J. M.; Gardner, P. *Analyst* **2007**, *132*, 750–755.

measurement geometry have received particular attention,[15,14] e.g., a transformation procedure to correct a dispersive phase error has been proposed.[13] However, no study in the literature has rigorously addressed the cause of apparent spectral artifacts and morphological distortions from first principles as a function of the microscope design and sample parameters. This situation is in sharp contrast to, for example, fluorescence microscopy, where the theory is highly sophisticated and numerical corrections to the data can be confidently made.[16−20]

Considerable care must be taken in applying the methods of analysis from visible microscopy to infrared microspectroscopy. Fluorescent emissions from distinct positions within the sample are uncorrelated, for example, allowing relatively simple modeling of image formation. In the visible and near-IR spectral regions, samples typically exhibit weak and/or broad absorbance profiles and the dominant intrinsic optical process is scattering. Hence, the usual approach is to describe the sample as a collection of nondispersive scattering inhomogeneities. In the mid-IR, however, fundamental vibrational modes of molecular species are resonant with the optical frequencies of the incident radiation. These resonances lead to sharp and strong absorption features that, of course, form the very basis of spectroscopy. As a consequence, the imaginary (absorptive) part of the refractive index is significant and the real part of the index undergoes a large anomalous dispersion.[21] It is this interplay of absorption (the contrast mechanism in IR spectroscopy), anomalous dispersion, and optical energy transport that, in part, leads to complications in recording and understanding of data.

In this manuscript, rigorous optical theory is developed for IR microspectroscopy. The analysis will enable an understanding of the relationship between properties of the sample and recorded data and will enable quantitative, instrument independent, and sample-geometry independent data interpretation. While the scope is limited to point microscopy of samples with simple layered structure (i.e., no transverse variation) in this manuscript, it is demonstrated that significant spectral differences from bulk measurements and significant spectral distortions may arise. When nontrivial transverse sample structure or morphology is considered, the situation becomes more complicated and that case is addressed in the follow-up article.[22] Hence, this manuscript serves both to help in understanding the sample−instrument effects for homogeneous samples and as a basis for further development of IR microspectroscopy theory for complex sample morphologies.

The following sections first describe the development of a mathematical model for point microspectroscopy. A planewave solution of Maxwell's equations is found for the sample−instrument system, and this solution is used to construct a focused-field solution. Next, numerical simulations are presented to systemati-
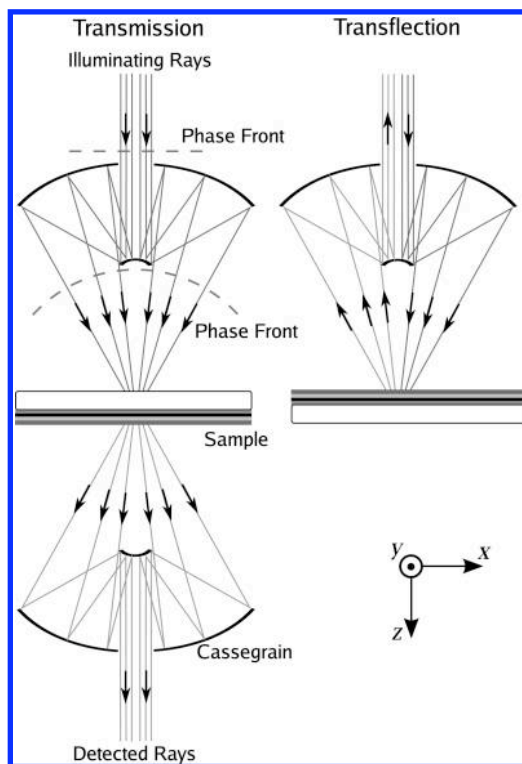

Figure 1. Illustration of focusing transmission and transflection optics. Cassegrains are used to focus light illuminating the sample and to collect the light to be detected. Loci of constant ray length are illustrated (− − −) and represent optical phase fronts. The locus above the upper Cassegrain can be regarded as an entrance pupil, and the loci below the upper Cassegrain can be regarded as an exit pupil. Note that for notational consistency, the illuminating light is always considered to originate from above the sample (i.e., from the z direction). The standard transmission case, where the sample is illuminated from underneath, through the substrate,[25] may be modeled using reciprocity[24] or by inverting the sample−substrate system, as illustrated. In this illustration, and in the numerical simulations that follow, the objective and condenser Cassegrains are assumed to be matched, although the theory presented is general and can account for mismatched Cassegrains.

cally examine the effects of focusing, dispersion, and sample structure. The model is also experimentally validated on a benchmarking sample.

THEORETICAL MODEL

Two generic optical systems for microspectroscopy are illustrated in Figure 1. The condensing optics focus light onto a sample supported by a planar substrate. The sample is assumed to be a layered medium without transverse structure. The resulting planar geometry, with transverse translational invariance, admits a relatively simple solution of Maxwell's equations,[23] and boundary conditions can be used to specify an incoming field consistent with focusing. As illustrated in Figure 1, transmission and transflection geometries are considered. While many IR microscopes are bottom illuminated for transmission and top illuminated for transflection, here top illumination is considered for both cases, in order to align the analytical treatment. It must be noted that the transmission case is directionally invariant

(15) Bassan, P.; Byrne, H. J.; Lee, J.; Bonnier, F.; Clarke, C.; Dumas, P.; Gazi, E.; Brown, M. D.; Clarke, N. W.; Gardner, P. *Analyst* **2009**, *134*, 1171–1175.
(16) Hiraoka, Y.; Sedat, J. W.; Agard, D. A. *Science* **1987**, *238*, 36–41.
(17) McNally, J. G.; Karpova, T.; Cooper, J.; Conchello, J. A. *Methods* **1999**, *19*, 373–385.
(18) Hell, S. W. *Nat. Biotechnol.* **2003**, *21*, 1347–1355.
(19) Gustafsson, M. G. L. *Proc. Natl. Acad. Sci. U.S.A.* **2005**, *102*, 13081–13086.
(20) Rust, M. J.; Bates, M.; Zhuang, X. *Nat. Methods* **2006**, *3*, 793–795.
(21) Yamamoto, K.; Ishida, H. *Vib. Spectrosc.* **1994**, *8*, 1–36.
(22) Davis, B. J.; Carney, P. S.; Bhargava, R. *Anal. Chem.* DOI: 10.1021/ac902068e.

(23) Born, M.; Wolf, E. *Principles of Optics*, 6th ed.; Cambridge University Press: Cambridge, U.K., 1980.

for these samples,[24] hence there is no loss of generality in considering top illumination.

The electromagnetic field in each layer of the sample–instrument system may be described using planewaves which satisfy both the boundary conditions and Maxwell's equations. This type of planewave analysis[26] is commonly encountered in many fields, including the design of antireflection coatings and Fabry–Perot interferometers. In contrast to many such analyses in the visible region of the spectrum, it is necessary to consider both the real (dispersive) and imaginary (absorptive) parts of the refractive index here. The focused field is constructed as a sum of planewaves incident from the diversity of angles dictated by the focusing optics. Each planewave can be propagated through the layered sample and substrate independently in this construction, generalizing the approach of Török et al.[27] Thus, the response of the system to a single incident plane wave is addressed first, then the incident focused field is described and, finally, the total resulting measurement is predicted.

Planewave Solutions. A Cartesian coordinate system is chosen with the z axis perpendicular to the planar boundaries between sample layers. Position vectors are written $\mathbf{r} = (x, y, z)^T$ where a superscript T denotes the vector transpose. Optical fields are represented by complex amplitudes at each temporal harmonic frequency $c\bar{\nu}$ where c is the speed of light in free space and $\bar{\nu}$ is the free space wavenumber. The permittivity and permeability of free space are denoted ε_0 and μ_0, respectively. It is assumed that the media in all layers are linear, isotropic, nonmagnetic (the relative permeability is unity), and contains no free charge. The relative permittivity $\varepsilon(\bar{\nu})$ or, equivalently, the real and imaginary (absorptive) parts of the refractive index ($n(\bar{\nu})$ and $k(\bar{\nu})$, respectively), vary from layer to layer. A single complex planewave[23] is then described by electric and magnetic fields of the respective forms

$$\mathbf{E}(\mathbf{r}, \bar{\nu}, t) = \mathbf{E}_0 \exp(i2\pi\bar{\nu}\mathbf{s}\cdot\mathbf{r}) \exp(-i2\pi\bar{\nu}ct) \qquad (1)$$

$$\mathbf{H}(\mathbf{r}, \bar{\nu}, t) = \sqrt{\frac{\varepsilon_0}{\mu_0}}(\mathbf{s}\times\mathbf{E}_0) \exp(i2\pi\bar{\nu}\mathbf{s}\cdot\mathbf{r}) \exp(-i2\pi\bar{\nu}ct) \qquad (2)$$

where $\mathbf{E}_0$ is the planewave amplitude vector, and $\mathbf{s}$ is a vector determining the direction of propagation and any absorptive or evanescent decay of the field. The vector $\mathbf{s} = (s_x, s_y, s_z)^T$ obeys the dispersion relation

$$s_x^2 + s_y^2 + s_z^2 = \varepsilon(\bar{\nu}) = [n(\bar{\nu}) + ik(\bar{\nu})]^2 \qquad (3)$$

For convenience, the time harmonic factors $\exp(-i2\pi\bar{\nu}ct)$ in eqs 1 and 2 are suppressed for the remainder of this article.

Samples for infrared microspectroscopy are typically mounted on a substrate and are present in air. Hence, a homogeneous sample may be considered to be a multilayer structure in which the sample, substrate, and air form a three layer system. For

convenience, the effects of atmospheric absorption are neglected here. To generalize, the model system consists of L layers, each parallel to the $x-y$ plane. In each layer, the field may be written as a superposition of planewaves of the form described above, the so-called angular spectrum.[23] The electric field in the ℓ th layer, that is in the z interval between the boundaries $z^{(\ell-1)}$ and $z^{(\ell)}$ (where $z^{(\ell)} > z^{(\ell-1)}$), is given by the sum over all components of the planewave angular spectrum in the slab,

$$\mathbf{E}^{(\ell)}(x, y, z, \bar{\nu}) = \bar{\nu} \int \int_{\mathbb{R}^2} \{\mathbf{B}^{(\ell)}(s_x, s_y, \bar{\nu}) \exp[i2\pi\bar{\nu}s_z^{(\ell)}(z - z^{(\ell-1)})] +$$
$$\hat{\mathbf{B}}^{(\ell)}(s_x, s_y, \bar{\nu}) \exp[-i2\pi\bar{\nu}s_z^{(\ell)}(z - z^{(\ell)})]\} \times$$
$$\exp[i2\pi\bar{\nu}(s_x x + s_y y)] \, ds_x \, ds_y \qquad (4)$$

where, by eq 3,

$$s_z^{(\ell)} = \sqrt{[n^{(\ell)}(\bar{\nu}) + ik^{(\ell)}(\bar{\nu})]^2 - s_x^2 - s_y^2} \qquad (5)$$

The principal value of the square root is taken by definition, so that the downward-propagating angular spectrum $\mathbf{B}^{(\ell)}(s_x, s_y, \bar{\nu})$ and the upward-propagating angular spectrum $\hat{\mathbf{B}}^{(\ell)}(s_x, s_y, \bar{\nu})$ must be explicitly distinguished in eq 4. The factor of $\bar{\nu}$ is included to ensure that angular spectra constant in $\bar{\nu}$ produces a power spectrum also constant in $\bar{\nu}$. Also note that the downward propagating light, described by $\mathbf{B}^{(\ell)}(s_x, s_y, \bar{\nu})$, is referenced to the upper boundary of the layer $z^{(\ell-1)}$, and the upward propagating light, described by $\hat{\mathbf{B}}^{(\ell)}(s_x, s_y, \bar{\nu})$, is referenced to the lower boundary of the layer $z^{(\ell)}$.

The field in the sample is determined by the field incident from the focusing optics, i.e., by $\mathbf{B}^{(1)}(s_x, s_y, \bar{\nu})$. This field appears in eq 4 referenced to an arbitrary plane $z^{(0)}$ that does not correspond to a layer boundary but is instead chosen for convenience. Boundary conditions relate the incident field to the field in each layer of the sample and to the field in the substrate. Maxwell's equations dictate these boundary conditions and also require transversality of the field in each layer. Explicitly, Gauss' equation $\nabla\cdot\mathbf{E}(\mathbf{r}, \bar{\nu}, t) = 0$, results in the constraints

$$s_x B_x^{(\ell)}(s_x, s_y, \bar{\nu}) + s_y B_y^{(\ell)}(s_x, s_y, \bar{\nu}) + s_z^{(\ell)} B_z^{(\ell)}(s_x, s_y, \bar{\nu}) = 0 \qquad (6)$$

and

$$s_x \hat{B}_x^{(\ell)}(s_x, s_y, \bar{\nu}) + s_y \hat{B}_y^{(\ell)}(s_x, s_y, \bar{\nu}) - s_z^{(\ell)} \hat{B}_z^{(\ell)}(s_x, s_y, \bar{\nu}) = 0 \qquad (7)$$

The requirement that the transverse components of $\mathbf{E}(\mathbf{r}, \bar{\nu}, t)$ and $\mathbf{H}(\mathbf{r}, \bar{\nu}, t)$ are continuous across layer boundaries couples plane wave components with the same arguments $(s_x, s_y, \bar{\nu})$, across layers via the constraints

$$B_x^{(\ell)} \exp[i2\pi\bar{\nu}s_z^{(\ell)}(z^{(\ell)} - z^{(\ell-1)})] + \hat{B}_x^{(\ell)} =$$
$$B_x^{(\ell+1)} + \hat{B}_x^{(\ell+1)} \exp[-i2\pi\bar{\nu}s_z^{(\ell+1)}(z^{(\ell)} - z^{(\ell+1)})] \qquad (8)$$

(24) Potton, R. J. *Rep. Prog. Phys.* **2004**, *67*, 717–754.
(25) Carr, G. L. *Rev. Sci. Instrum.* **2001**, *72*, 1613–1619.
(26) Yeh, P. *Optical Waves in Layered Media*, 2nd ed.; Wiley-Interscience: Hoboken, NJ, 2005.
(27) Török, P.; Varga, P.; Laczik, Z.; Booker, G. R. *J. Opt. Soc. Am. A* **1995**, *12*, 325–332.

$$B_y^{(l)} \exp\left[i2\pi\bar{\nu}s_z^{(l)}(z^{(l)} - z^{(l-1)})\right] + \hat{B}_y^{(l)} =$$
$$B_y^{(l+1)} + \hat{B}_y^{(l+1)}\exp\left[-i2\pi\bar{\nu}s_z^{(l+1)}(z^{(l)} - z^{(l+1)})\right] \quad (9)$$

$$\left(s_y B_z^{(l)} - s_z^{(l)} B_y^{(l)}\right) \exp\left[i2\pi\bar{\nu}s_z^{(l)}(z^{(l)} - z^{(l-1)})\right] +$$
$$\left(s_y \hat{B}_z^{(l)} + s_z^{(l)} \hat{B}_y^{(l)}\right) = \left(s_y B_z^{(l+1)} - s_z^{(l+1)} B_y^{(l+1)}\right) +$$
$$\left(s_y \hat{B}_z^{(l+1)} + s_z^{(l+1)} \hat{B}_y^{(l+1)}\right) \exp\left[-i2\pi\bar{\nu}s_z^{(l+1)}(z^{(l)} - z^{(l+1)})\right] \quad (10)$$

$$\left(s_z^{(l)} B_x^{(l)} - s_x B_z^{(l)}\right) \exp\left[i2\pi\bar{\nu}s_z^{(l)}(z^{(l)} - z^{(l-1)})\right] +$$
$$\left(-s_z^{(l)} \hat{B}_x^{(l)} - s_x \hat{B}_z^{(l)}\right) = \left(s_z^{(l+1)} B_x^{(l+1)} - s_x B_z^{(l+1)}\right) +$$
$$\left(-s_z^{(l+1)} \hat{B}_x^{(l+1)} - s_x \hat{B}_z^{(l+1)}\right) \exp\left[-i2\pi\bar{\nu}s_z^{(l+1)}(z^{(l)} - z^{(l+1)})\right] \quad (11)$$

For fixed arguments $(s_x, s_y, \bar{\nu})$ there are $6L$ unknowns, $3L$ for $\mathbf{B}^{(l)}$ $(s_x, s_y, \bar{\nu})$ and $3L$ for $\hat{\mathbf{B}}^{(l)}$ $(s_x, s_y, \bar{\nu})$. The transversality conditions of eqs 6 and 7 provide $2L$ linearly independent equations (one pair for each layer) and the boundary conditions of eqs 8−11 provide $4(L-1)$ linearly independent equations (four equations for each boundary). The remaining degrees of freedom allow for the specification of the incident (incoming) field at the top and bottom layers. At the last boundary, the $z = z^{(L-1)}$ plane, the field is assumed to be strictly outgoing, i.e., the incoming field is zero. Thus, it is required that

$$\hat{\mathbf{B}}^{(L)}(s_x, s_y, \bar{\nu}) = \mathbf{0} \quad (12)$$

As a result, there are only two degrees of freedom in the system, which are identified with the electric field amplitude of the illumination.

The total field is linear in the values of the illuminating field $\mathbf{B}^{(1)}(s_x, s_y, \bar{\nu})$; hence, it is instructive to consider as an example the case of single-planewave illumination, as shown in Figure 2. Notice that the coherent superposition of transmitted and reflected fields produces interference patterns in the sample and that the absorption in the sample results in decaying amplitudes into the media. These effects are also important in the case where the incident field consists of a superposition of planewaves that form a focus.

As seen in Figure 2, enforcing eqs 6−11 results in a solution where transmission, reflection, and interference effects all play a role. However, if two boundaries are separated by a large distance, the exponential factors in eqs 8−11 will result in a solution that varies rapidly with a small change in the wavelength, i.e., the interference effects will change rapidly as a function of $\bar{\nu}$. Such a situation arises when light propagates through a mounting substrate with a thickness much greater than a wavelength. This type of highly oscillatory spectral behavior will not be resolved by the spectrometer, meaning that the interference effects from the thick layer will not be observed in the data. Hence, in transmission mode, the effect of the mounting substrate can be accurately described by modeling the distant substrate−air boundary as uncoupled to the closely spaced boundaries, i.e., those associated with the sample. Thus eqs 6−11 need only to be solved for closely spaced boundaries (the air−sample and the sample−substrate boundaries), and the resulting field of interest can otherwise be propagated through the distant boundary using standard transmission coefficients.

Focused Illumination. While the previous subsection has illustrated the interaction of planewave fields with a sample,
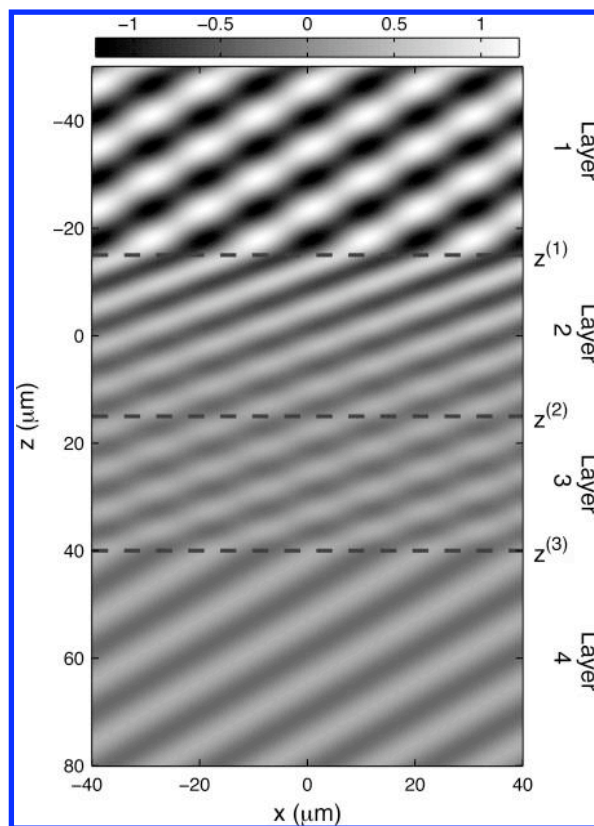

Figure 2. An example of the field produced in a layered sample under unit-amplitude planewave illumination. The illuminating light is incident at an angle of 45 in the $x-z$ plane, is purely y-polarized and has a wavelength of 10 μm in free space. The real part of the complex representation of the field is displayed. The indices of the four media present are, from top to bottom, 1, 1.4 + 0.05i, 1.4, and 1. The boundaries of the media are marked with dashed lines.

microspectroscopy involves the use of focusing optics to localize signal and increase local throughput. Focusing optics can be modeled using geometrical optics techniques such as ray tracing. In this paradigm, the Cassegrain arrangement that is usually employed for focusing in the mid-IR maps a ray on the entrance pupil to a focused ray on the exit pupil as illustrated in Figure 3. It should be noted that the locus described as the exit pupil will intersect rays emerging from the Cassegrain when the Cassegrain is used as a condenser but will intersect incoming rays when the Cassegrain is used for collection (i.e., as an objective).

The angular spectrum amplitudes of the focused, illuminating field, $\mathbf{B}^{(1)}(s_x, s_y, \bar{\nu})$, can be associated with rays in the exit pupil.[28] As illustrated in Figure 3, the vector elements s_x and s_y determine not only the propagation direction of a focused ray but also the intersection of the associated ray path and the entrance pupil. The field in the pupil can therefore be expressed as a vector function $\mathbf{P}(s_x, s_y, \bar{\nu})$. A matrix $C_I(s_x, s_y, \bar{\nu})$ relates $\mathbf{P}(s_x, s_y, \bar{\nu})$ to $\mathbf{B}^{(1)}(s_x, s_y, \bar{\nu})$ and explicitly accounts for the optical elements (i.e., the Cassegrain) in the system,

$$\mathbf{B}^{(1)}(s_x, s_y, \bar{\nu}) = C_I(s_x, s_y, \bar{\nu})\mathbf{P}(s_x, s_y, \bar{\nu}) \quad (13)$$

(28) Wolf, E. *Proc. R. Soc. London, Ser. A: Math. Phys. Sci.* **1959**, *253*, 349–357.
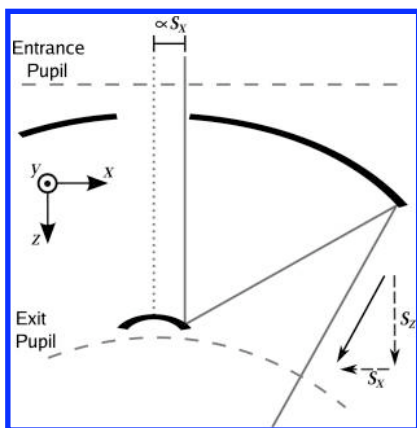
Figure 3. An illustrative ray path through a Cassegrain system. Mirrors (heavy lines) reflect rays parallel to the z axis at the entrance pupil to rays at the exit pupil which are directed to the focal point. The vector **s** gives the propagation direction for a ray and, for an aplanatic system, the transverse component of this vector (s_x in this two-dimensional figure) is proportional to the transverse position at which the ray intersects the entrance pupil. The ray path for $s_x = 0$ is represented by the dotted line; in a Cassegrain, this ray does not contribute to the focused field.

The case of a lossless aplanatic focusing system has been addressed by Richards and Wolf,[29] and results from their work can be used to find $C_I(s_x, s_y, \bar{\nu})$.

The construction of $C_I(s_x, s_y, \bar{\nu})$ is most easily accomplished by defining polarization basis vectors before and after the Cassegrain, namely, the transverse-electric (s-polarized) and transverse-magnetic (p-polarized) vectors. Assuming that the Cassegrain(s) is in free space, these vectors are

$$\mathbf{v}_s' = \mathbf{v}_s = \frac{1}{\sqrt{s_x^2 + s_y^2}}(-s_y, s_x, 0)^{\mathrm{T}} \qquad (14)$$

$$\mathbf{v}_p = \frac{1}{\sqrt{s_x^2 + s_y^2}}(-s_x, -s_y, 0)^{\mathrm{T}} \qquad (15)$$

$$\mathbf{v}_p' = \frac{1}{\sqrt{s_x^2 + s_y^2}}(-s_x s_z^{(1)}, -s_y s_z^{(1)}, s_x^2 + s_y^2)^{\mathrm{T}} \qquad (16)$$

where a prime indicates a vector on the exit pupil side of the Cassegrain and no prime indicates the entrance pupil side. Since the focusing is performed in free space and only propagating waves are produced, $s_x^2 + s_y^2 \leq 1$, and s_x, s_y, and $s_z^{(1)}$ are all real.

The field on the exit pupil $\mathbf{P}'(s_x, s_y, \bar{\nu})$ can be found by mapping each ray through the focusing optics and correctly accounting for conservation of energy.[29] With neglect of the constant phase factors,

$$\mathbf{P}'(s_x, s_y, \bar{\nu}) = \sqrt{s_z^{(1)}}[\mathbf{v}_s'\mathbf{v}_s^{\mathrm{T}} + \mathbf{v}_p'\mathbf{v}_p^{\mathrm{T}}]\mathbf{P}(s_x, s_y, \bar{\nu}) \qquad (17)$$

The field on the exit pupil can then be used to determine the resulting angular spectrum[28]

(29) Richards, B.; Wolf, E. *Proc. R. Soc. London, Ser. A: Math. Phys. Sci.* **1959**, *253*, 358–379.

$$\mathbf{B}^{(1)}(s_x, s_y, \bar{\nu}) = \frac{\zeta \mathbf{P}'(s_x, s_y, \bar{\nu})}{s_z^{(1)}} \qquad (18)$$

where ζ is the focal length of the Cassegrain. The description of the focusing optics then takes the form,

$$C_I(s_x, s_y, \bar{\nu}) = f_s(s_x, s_y, \bar{\nu})\mathbf{v}_s'\mathbf{v}_s^{\mathrm{T}} + f_p(s_x, s_y, \bar{\nu})\mathbf{v}_p'\mathbf{v}_p^{\mathrm{T}} \qquad (19)$$

and in the lossless aplanatic case,

$$f_s(s_x, s_y, \bar{\nu}) = f_p(s_x, s_y, \bar{\nu}) \propto \frac{\zeta}{\sqrt{s_z^{(1)}}} \qquad (20)$$

More generally, $f_s(s_x, s_y, \bar{\nu})$ and $f_p(s_x, s_y, \bar{\nu})$ can be modified to capture losses, aberrations, and the central obstruction in the Cassegrain. Note that it is implicit in this treatment that the illumination reference plane $z^{(0)}$ is the focal plane for a focus formed in free space. It can also be seen, from eq 19 that $\mathbf{B}^{(1)}(s_x, s_y, \bar{\nu})$ obeys the transversality condition of eq 6. Examples of focused angular spectra, with the central Cassegrain obstruction included, are shown in Figure 4.

In free space, the illuminating angular spectrum $\mathbf{B}^{(1)}(s_x, s_y, \bar{\nu})$ completely defines the field. The presence of the layered sample alters the field in a manner that may be calculated for each planewave component separately, as described above. The resultant focused field is then found by summing the planewave contributions in the resulting angular spectra. An example of a field focused into a layered sample is shown in Figure 5.

The analysis to this point has addressed a planewave normally incident on the entrance of the condenser Cassegrain. At close to normal incidence, a slightly off-axis illumination results in the field
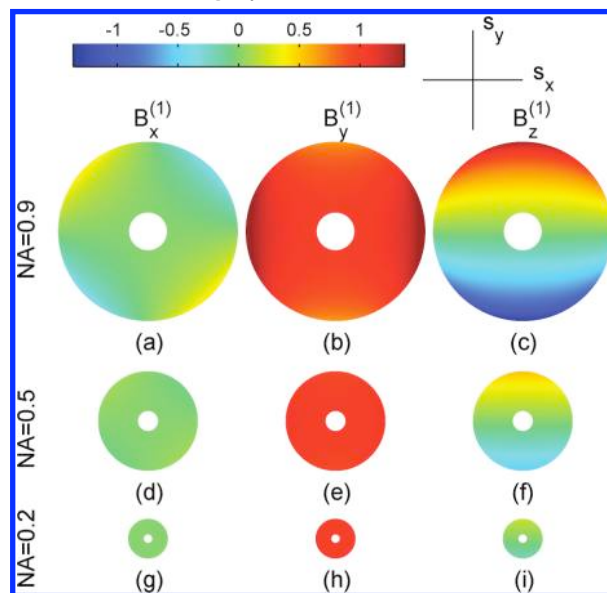

Figure 4. Normalized angular spectra $\mathbf{B}^{(1)}(s_x, s_y, \bar{\nu})$ resulting from a y-polarized planewave on the entrance pupil. The (a,d,g) x components, (b,e,h) y components, and (c,f,i) z components of $\mathbf{B}^{(1)}(s_x, s_y, \bar{\nu})$ are plotted separately. Focusing numerical apertures (NAs) of (a–c) 0.9, (d–f) 0.5, and (g–i) 0.2 are illustrated, and in each case the NA of the central obstruction is 20% of the total NA. Note that for large apertures, the y-polarized field on the entrance pupil produces significant x- and z-directed fields on the exit pupil. In transflection mode, one-half of the apertures above would be used for illumination, with the other half reserved for collection.

$$\mathbf{P}(s_x, s_y, \bar{v}) \approx \mathbf{P}_0(s_x, s_y, \bar{v}) \exp[-i2\pi\bar{v}(s_x x_o + s_y y_o)] \qquad (21)$$

at the entrance pupil, where x_o and y_o determine the inclination of the beam and the normally incident field is $\mathbf{P}_0(s_x, s_y, \bar{v})$. Carrying the illumination of eq 21 through eqs 13 and 4 shows that the inclination will have the effect of spatially displacing the focused field by $\mathbf{r}_o = (x_o, y_o, 0)^T$. In this manner, the angle of incidence of light on the entrance pupil governs the transverse position of the focused field. The use of aplanatic optics gives minimal distortions in the translated field.[23]

In widefield imaging, light is incident on the illumination Cassegrain at a range of angles simultaneously. Fields associated with distinct illumination angles are generally statistically uncorrelated, meaning that each can be considered individually. The resultant intensities on the detector (see the following subsection) sum, without interfering, in the process of data collection. Similarly, for unpolarized illumination, an x-polarized illumination field and a y-polarized illumination are present simultaneously. Each of these can also be analyzed independently and the measured intensity of each summed (an incoherent sum) to give the total signal.

Detection. The field at the detector may be related to the field emerging from the sample in much the same way that the illuminating field is found from the field in the entrance pupil. In transmission mode, the field exiting the Cassegrain objective, denoted $\mathbf{Q}(s_x, s_y, \bar{v})$, is dependent on the emerging angular spectrum $\mathbf{B}^{(L)}(s_x, s_y, \bar{v})$. Similar to eq 13,
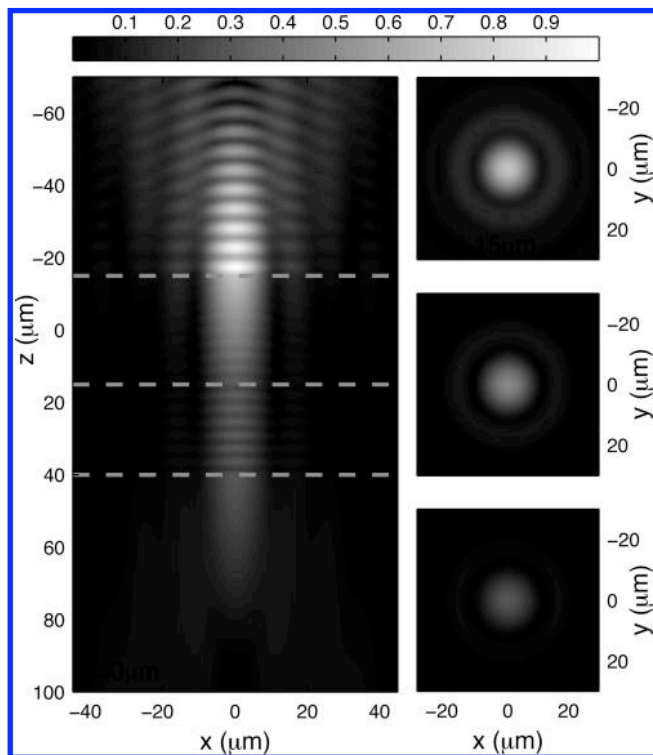

Figure 5. The focused field magnitude $|\mathbf{E}(x, y, z, \bar{v})|$ for $\bar{v} = 1000$ cm^{-1} (a free space wavelength of 10 μm), the four-layer object of Figure 2 and the angular planewave spectrum of Figure 4d−f plotted on a normalized scale. The free space focal plane is at $z^{(0)} = 0$. One transverse−axial (x−z) section is plotted at $y = 0$ and three transverse−transverse (x−y) sections are plotted at $z = -15$ μm, $z = 0$, and $z = 15$ μm. In this example, the Cassegrain pupil is filled, i.e., there are no apertures limiting the width of the illuminating beam before the focusing optics.

$$\mathbf{Q}(s_x, s_y, \bar{v}) = C_T(s_x, s_y, \bar{v})\mathbf{B}^{(L)}(s_x, s_y, \bar{v}) \qquad (22)$$

In the transflection mode, the field exiting the sample is the upward propagating field determined by the angular spectrum $\hat{\mathbf{B}}^{(1)}(s_x, s_y, \bar{v})$ and

$$\mathbf{Q}(s_x, s_y, \bar{v}) = C_R(s_x, s_y, \bar{v})\hat{\mathbf{B}}^{(1)}(s_x, s_y, \bar{v}) \qquad (23)$$

As with the illumination matrix $C_I(s_x, s_y, \bar{v})$, the matrices $C_T(s_x, s_y, \bar{v})$ and $C_R(s_x, s_y, \bar{v})$ describe the focusing optics for each case. In transmission, $C_T(s_x, s_y, \bar{v})$ describes focusing of the downward propagating light transmitted through the sample and substrate, while in transflection $C_R(s_x, s_y, \bar{v})$ describes the focusing of the upward propagating reflected light.

The angular spectra emerging from the sample define the field incident on the objective Cassegrain. Similar to eq 18, this incident field can be expressed as $\mathbf{Q}'(s_x, s_y, \bar{v}) = \mathbf{B}^{(L)}(s_x, s_y, \bar{v})s_z^{(L)}/\zeta$ in transmission mode and as $\mathbf{Q}'(s_x, s_y, \bar{v}) = \mathbf{B}^{(1)}(s_x, s_y, \bar{v})s_z^{(1)}/\zeta$ in transflection mode. The mapping of the diverging field $\mathbf{Q}'(s_x, s_y, \bar{v})$ through an ideal objective Cassegrain to the collimated field $\mathbf{Q}(s_x, s_y, \bar{v})$ obeys the same relation as was given in the illumination case, i.e., eq 17. Assuming that the last layer of the system is free-space, the transmission mode relation $C_T(s_x, s_y, \bar{v})$ may therefore be represented compactly in the bases defined in eqs 14−16,

$$C_T(s_x, s_y, \bar{v}) = f'_s(s_x, s_y, \bar{v})\mathbf{v}_s(\mathbf{v}'_s)^T + f'_p(s_x, s_y, \bar{v})\mathbf{v}_p(\mathbf{v}'_p)^T \qquad (24)$$

where

$$f'_s(s_x, s_y, \bar{v}) = f'_p(s_x, s_y, \bar{v}) \propto \frac{\sqrt{s_z^{(1)}}}{\zeta} \qquad (25)$$

for the ideal Cassegrain objective. Notice that for transmission with no sample or substrate (the empty instrument case), $\mathbf{B}^{(L)}(s_x, s_y, \bar{v}) = \mathbf{B}^{(1)}(s_x, s_y, \bar{v})$, leading to the result $\mathbf{P}(s_x, s_y, \bar{v}) = \mathbf{Q}(s_x, s_y, \bar{v})$. This is to be expected; with no sample or substrate, propagation through the focusing system has no net effect.

In transflection mode a similar relation holds,

$$C_R(s_x, s_y, \bar{v}) = \hat{f}'_s(s_x, s_y, \bar{v})\hat{\mathbf{v}}_s(\hat{\mathbf{v}}'_s)^T + \hat{f}'_p(s_x, s_y, \bar{v})\hat{\mathbf{v}}_p(\hat{\mathbf{v}}'_p)^T \qquad (26)$$

where $\hat{f}'_s(s_x, s_y, \bar{v})$ and $\hat{f}'_p(s_x, s_y, \bar{v})$ are as in eq 25 for ideal collection, and the reflected s- and p-polarized basis vectors are given by the expressions

$$\hat{\mathbf{v}}_s = \hat{\mathbf{v}}'_s = \frac{1}{\sqrt{s_x^2 + s_y^2}}(-s_y, s_x, 0)^T \qquad (27)$$

$$\hat{\mathbf{v}}_p = \frac{1}{\sqrt{s_x^2 + s_y^2}}(s_x, s_y, 0)^T \qquad (28)$$

$$\hat{\mathbf{v}}'_p = \frac{1}{\sqrt{s_x^2 + s_y^2}}(s_x s_z^{(1)}, s_y s_z^{(1)}, s_x^2 + s_y^2)^T \qquad (29)$$

As before, a prime indicates a vector on the sample side of the Cassegrain.

To achieve magnification, the field $\mathbf{Q}(s_x, s_y, \bar{\nu})$ is focused on to a detector by a low-angle focusing system. For an imaging system with magnification of M, the field on the detector plane is given by

$$\mathbf{D}(x, y, \bar{\nu}) = \frac{\bar{\nu}}{M} \int \int_{\mathbb{R}^2} \mathbf{Q}(s_x, s_y, \bar{\nu}) \exp(i2\pi\bar{\nu}s_z^{(1)}z_d) \times$$
$$\exp\left[i2\pi\bar{\nu}\left(\frac{s_x}{M}x + \frac{s_y}{M}y\right)\right] \mathrm{d}s_x \, \mathrm{d}s_y, \quad (30)$$

where $s_z^{(1)}$ is calculated as in eq 5 but with magnified values s_x/M and s_y/M instead of s_x and s_y, and z_d is the offset between the detector plane and the focal plane. The focusing described in eq 30 is of the same form as in eq 4 but with the focused spectrum corresponding to $\mathbf{Q}(s_x, s_y, \bar{\nu})$, the field incident on the detector focusing optics. This is justified for the focusing onto the detector, as the fields on the entrance and exit pupils of the low-angle focusing system are approximately equal, i.e., the focusing tensor $C(s_x, s_y, \bar{\nu})$ is modeled as the identity operator. Note that $\mathbf{D}(x, y, \bar{\nu})$, the field incident on the detector, lies in the $x-y$ plane as $\mathbf{Q}(s_x, s_y, \bar{\nu})$ is spanned by $\mathbf{v}_s$ and $\mathbf{v}_p$ (see eqs 14, 15, 24, and 26).

The signal measured by an optical detector is proportional to the intensity of the field integrated over the detector area, i.e.,

$$\mathbb{I}(\bar{\nu}) = \int \int_{\Omega} |\mathbf{D}(x, y, \bar{\nu})|^2 \, \mathrm{d}x \, \mathrm{d}y \quad (31)$$

where Ω is the detector area. If the detector area is large compared to the focal spot, then the region of integration above can be replaced with the entire $x-y$ plane. In this case, Parseval's theorem can be applied to calculate the data in terms of the collimated beam exiting the Cassegrain objective, i.e., the data become independent of the focusing on to the detector with

$$\mathbb{I}(\bar{\nu}) = \int \int_{\mathbb{R}^2} |\mathbf{Q}(s_x, s_y, \bar{\nu})|^2 \, \mathrm{d}s_x \, \mathrm{d}s_y \quad (32)$$

Here the recorded signals are simply the total intensity of the collimated beam emerging from the collection Cassegrain.

Relating Theory to Current Practice. The molecular interpretation of recorded data in microspectroscopy typically follows that of bulk spectroscopy, in which the recorded signal intensity is often interpreted using the expression

$$\mathbb{I}_S(\bar{\nu}) = |\mathbf{P}(\bar{\nu})|^2 T_S(\bar{\nu})\exp[-4\pi\bar{\nu}k(\bar{\nu})b] \quad (33)$$

Here $\mathbf{P}(\bar{\nu})$ is the illumination field amplitude, b is the effective path length (nominally, the sample thickness for transmission and twice the sample thickness for the transflection measurements), and $T_S(\bar{\nu})$ describes a net transmission or reflection coefficient. To calculate absorption spectra, a background measurement is first obtained,

$$\mathbb{I}_0(\bar{\nu}) = |\mathbf{P}(\bar{\nu})|^2 T_0(\bar{\nu}) \quad (34)$$

where $T_0(\bar{\nu})$ describes the transmission and reflection effects for the experimental setup without the sample. The recorded absorbance, $A(\bar{\nu})$, is obtained from the normalized spectrum,

$$A(\bar{\nu}) = -\log_{10}\left[\frac{I_S(\bar{\nu})}{I_0(\bar{\nu})}\right]$$
$$= \frac{4\pi\bar{\nu}k(\bar{\nu})b}{2.303} - \log_{10}\left[\frac{T_S(\bar{\nu})}{T_0(\bar{\nu})}\right] \quad (35)$$

The molar absorptivity is defined as

$$a(\bar{\nu}) = \frac{4\pi\bar{\nu}k(\bar{\nu})}{2.303\rho} \quad (36)$$

where ρ is the concentration of the absorbing species. Finally, in the ideal case where the sample-free transfer function, $T_0(\bar{\nu})$, is equal to the transfer function with the sample, $T_S(\bar{\nu})$, Beer's law

$$A(\bar{\nu}) = a(\bar{\nu})b\rho \quad (37)$$

can be recovered from eq 35.

With comparison of eqs 35 and 37, it may be recognized that the recorded absorbance spectrum should be corrected for optical effects to recover analytically meaningful spectra that are independent of the instrument and the sample geometry. Comparing eq 33 with the rigorous model in the previous section, it should be noted that the simple model does not fully take into account the structure of the object (beyond the path length b) nor the real part of the refractive index. These two factors are known to lead to interference and dispersion effects in bulk-sample spectroscopy.[30,31] Restated, in the simple model the transmission or reflection coefficient $T_S(\bar{\nu})$ is considered to be independent of the sample geometry and the properties of the sample and substrate. The model of eq 33 also does not account for the angle(s) of illumination and detection, this can be particularly important in microspectroscopy, as focusing results in simultaneous illumination with waves of many incidence angles. The impact of neglecting these factors on the data is apparent in the simulations that follow. The various effects leading to spectral distortions are identified and systematically quantified through the use of the developed model.

In the rest of this article, the model described is first experimentally validated using a benchmarking sample. The effects of the focusing optics of the imaging system are then isolated in simulation by considering a hypothetical idealized sample that eliminates the sample-induced distortions described by the second term in eq 35. Transmission and transflection geometries using common substrates are then simulated and it is seen that transflection measurements in particular are susceptible to sample-induced distortions. These distortions are seen to be exacerbated if a substrate of intermediate index is used. Further sample-induced distortions are predicted if an air gap is present between the substrate and the sample. Finally, the correspondence between a simplified single-ray model and the fully focused model is examined.

(30) Allara, D. L.; Baca, A.; Pryde, C. A. *Macromolecules* **1978**, *11*, 1215–1220.
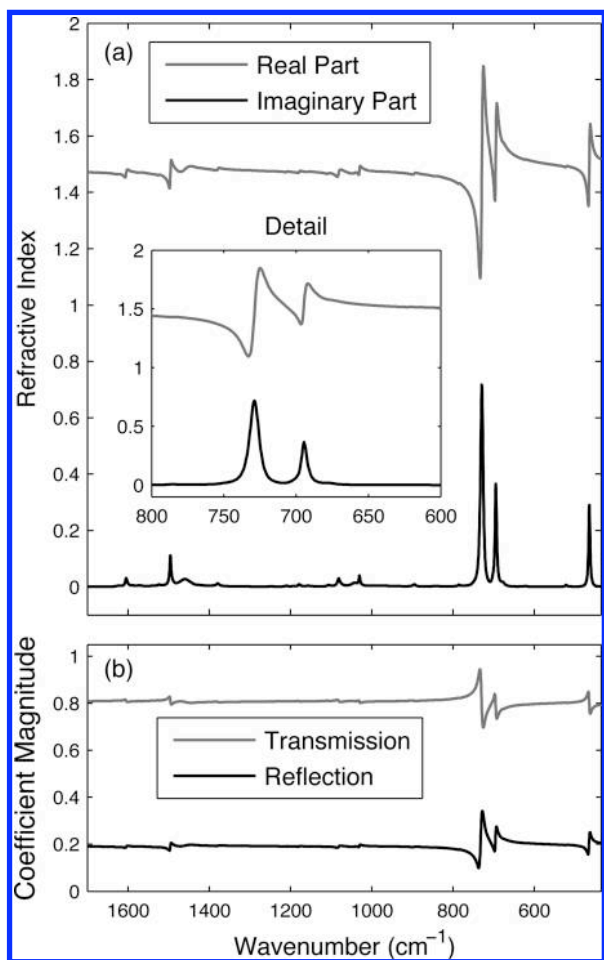(31) Zhang, Z. M. *J. Heat Transfer* **1997**, *119*, 645–647.

Figure 6. The (a) complex refractive index of toluene[32] and (b) the magnitude of the normal-incidence complex transmission and reflection coefficients for an air−toluene boundary. The Supporting Information includes graphs of the refractive indices of the other materials considered in this article.

To make predictions from the theoretical model, toluene is used as a homogeneous sample of interest. Toluene exhibits distinct and clearly identifiable absorption modes of varying strength over the entire mid-IR region, making it an ideal sample. In addition, toluene has a well characterized complex refractive index[32] [shown in Figure 6a] which is publicly available.[33] Refractive index changes and anomalous dispersion[34] in the vicinity of absorption peaks can be clearly observed [e.g., see inset in Figure 6a]. This variation of refractive index, in both the real and imaginary parts, affects the recorded data. A simple illustration of these effects is shown in Figure 6b, where the transmission and reflection coefficients at an air−toluene boundary can be seen to have structure influenced by the dispersive real index profile.

Experimental Validation of the Model. The model presented here was validated by performing microspectroscopy measurements on a well characterized benchmarking sample. The sample was designed such that both transmission and transflection measurements would result in significant signal. The model

should then be able to accurately predict both sets of data from a single description of the sample−substrate system.

The sample was prepared by first forming a thin (≈75 nm) germanium layer by sputter coating on a barium fluoride (BaF$_2$) disk. A common photoresist material, SU-8 2000.5 (MicroChem Corp., Newton, MA), was spin coated to an approximate thickness of 10 μm and pattern cured by UV exposure using a standard USAF 1951 target (Edmond Optics, Barrington, NJ). Postcuring, the entire sample was baked at 95 C and developed as per standard protocols.[35] A postbake at 150 C for 5 min was performed to ensure complete polymerization and long-term stability.

The sample data were recorded on a Varian Stingray system using a mid-IR interferometer and microscopy with glass apertures. A narrowband, liquid nitrogen cooled detector is used to record spectra. Data are recorded at an undersampling ratio of 2 referenced to the He−Ne laser, zero-filled by a factor of 2, and transformed using Happ−Genzel apodization. Single beam spectra acquired for the sample (a position near the center of a larger region of SU-8 and far from an transverse features) and background (a position with no SU-8) are subsequently converted to absorbance spectra. Both transmission and transflection mode data were acquired without perturbing the sample.

The SU-8 polymer is the sample layer to be characterized, while the refractive indices are known for the thin germanium[36] layer and the barium fluoride[37] substrate. Background single beam spectra, Figure 7d, are recorded on a region of the sample without SU-8, and the sample single beam spectra, Figure 7a, are recorded on a region of the sample with SU-8. If absorbance calculations are performed according to eq 35, the transmission and transflection results, plotted in Figure 7c, are not consistent. Significant interference effects are visible, and peak shapes, locations, and heights can be seen to differ significantly, despite the fact that the measurements were taken from the same sample.

To correctly interpret the data, it is necessary to include optical effects, as modeled in this work. As a first step, the source spectrum, $|\mathbf{P}(s_x, s_y, \bar{\nu})|^2$ was determined from the background measurement. It is assumed that the illumination is constant across the entrance pupil so that the spectrum is not dependent on s_x and s_y. The numerical aperture of the Cassegrain and the Cassegrain obstruction were found to be best modeled as 0.40 and 0.26, respectively. The expected reflection and transmission coefficients from the air, germanium, barium fluoride, air system were calculated using the microspectroscopy model and divided out (see eq 34). The resulting transmission and transflection single beam spectra of the source are shown in Figure 7g. Since the instrument uses different optical paths for the transmission and transflection measurements, these two source spectra cannot be expected to be equal or proportional. It can, however, be seen that the source spectral profiles are qualitatively consistent, which was not the case before transmission and reflection effects were considered, see Figure 7d.

Once the source profiles are established, a preliminary estimate of absorbance can be found. Data were predicted by modeling the sample index as purely real with $n_0(\bar{\nu}) = 1.4017$. The data

(32) Bertie, J. E.; Jones, R. N.; Apelblat, Y.; Keefe, C. D. *Appl. Spectrosc.* **1994**, *48*, 127–143.
(33) http://keefelab.cbu.ca/?page_id=19.
(34) Saleh, B. E. A.; Teich, M. C. In *Fundamentals of Photonics*; Wiley-Interscience: New York, 1991; Chapter 5, pp 176−179.
(35) Processing Guidelines for SU-8 Permanent Epoxy Negative Photoresist. http://www.microchem.com/products/pdf/SU-82000DataSheet2000thru2015Ver4.pdf.
(36) Barnes, N. P.; Piltch, M. S. *J. Opt. Soc. Am.* **1979**, *69*, 178–180.
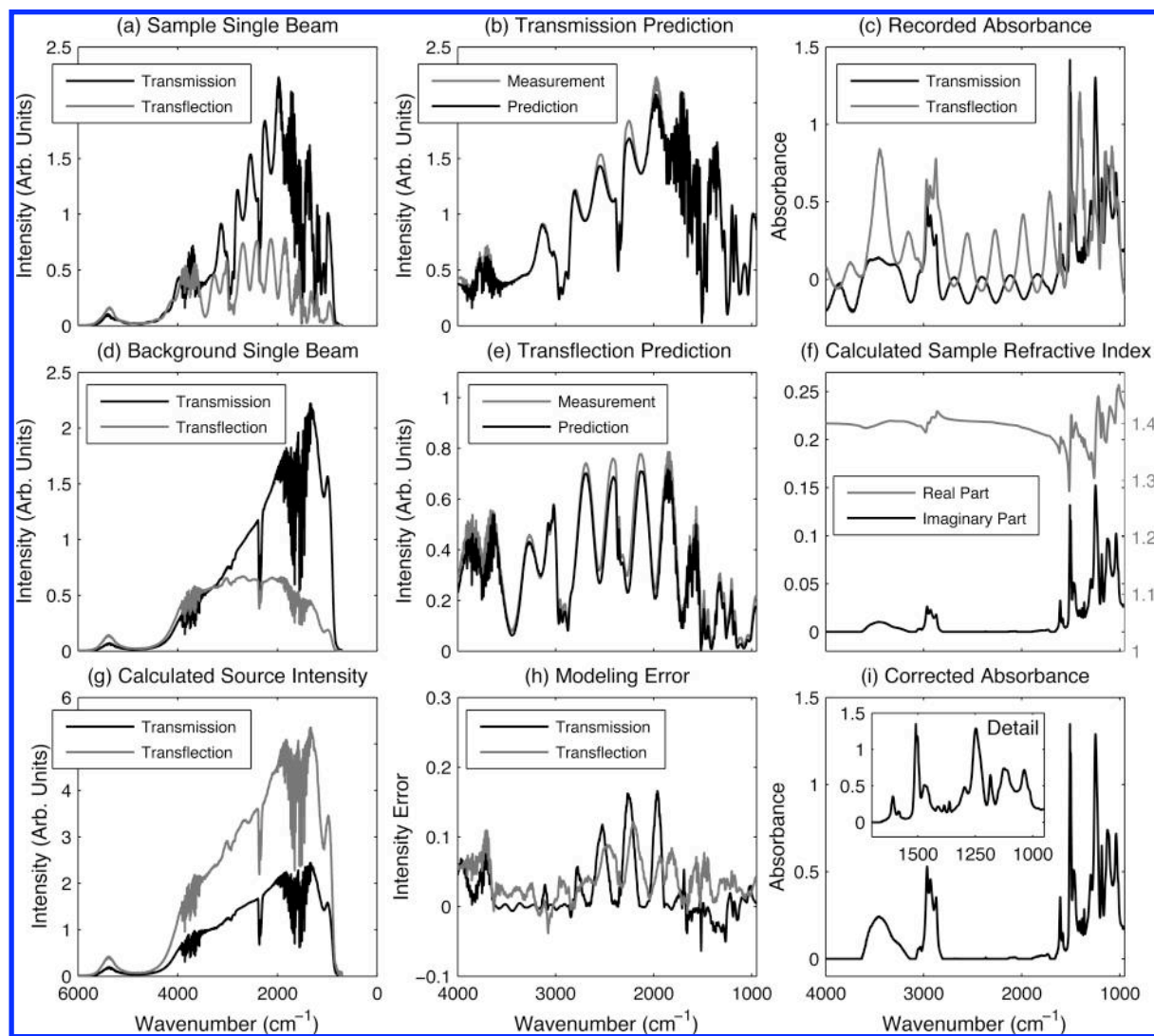(37) Malitson, I. H. *J. Opt. Soc. Am.* **1964**, *54*, 628–632.

Figure 7. Experimental data and quantities used in the modeling of the benchmarking sample: (a) the measured single beam spectra for the substrate and sample (SU-8 polymer layer), (d) the measured single beam spectra for the substrate alone, (c) the absorbance as calculated from the ratios of the single beam spectra using eq 35, (g) the source spectra $|\mathbf{P}(\bar{v})|^2$, as calculated by compensating the background spectra for the effects of the substrate, (b) the single beam transmission spectrum predicted by the model, compared to that measured, (e) the single beam transflection spectrum predicted by the model, compared to that measured, (f) the residual differences between the plots in parts b and e, (f) the complex refractive index calculated using the microspectroscopy model and Kramers−Kronig analysis, (i) the recovered absorbance of SU-8, as calculated using the imaginary part of the refractive index shown in part f and eq 35.

predicted from the uniform index were used as an improved background measurement which captures interference effects, such as those seen in Figure 7a but not in the original background measurement of Figure 7d. With the use of eq 35, an estimate of the imaginary index $k(\bar{v})$ can be found from the transmission data. Applying a Kramers−Kronig calculation[38] to $k(\bar{v})$ gives an estimate of the variations of $n(\bar{v})$ about the underlying constant value $n_0(\bar{v})$. The estimate of the refractive index, $n(\bar{v}) + ik(\bar{v})$, is then used to predict the single beam transmission spectrum. The difference between this prediction and the measurement is then used to update the absorbance and hence the imaginary index $k(\bar{v})$. By iteration of the algorithmic cycle, (1) update the absorbance estimate from the difference between the measured and predicted transmission data; (2) calculate the complex refractive index from the absorbance using Kramers−Kronig analysis; (3) calculate the

predicted transmission data using the model and the complex refractive index of the polymer, it is possible to converge on the complex refractive index of the polymer.[39,40]

The resulting complex index is plotted in Figure 7f and is used to predict spectra for both transmission and transflection modes. A good agreement, Figure 7b,e,h, is observed between the predicted and observed data for both transmission and transflection. The errors that are observed can likely be attributed to factors such as sample variations, unmodeled elements in the instrument optical path, and/or sample tilt. In Figure 7i the absorbance spectrum, free of optical effects, as calculated from the recorded data is shown. The agreement between predictions and measurements validates the model by demonstrating predictive power based on a physical description of the sample.

In modeling the measurement of the benchmarking sample, the refractive index of the cross-linked SU-8 layer was estimated. This estimate shows good consistency with the noncross-linked

(38) Kuzmenko, A. B. *Rev. Sci. Instrum.* **2005**, *76*, 083108.

SU-8 measurements that appear in the literature.[41,42] It should also be noted that the background value of the refractive index, $n_0(\bar{v})$, the exact thicknesses of the SU-8 layer (12.43 μm), and the exact thickness of the germanium layer (79 nm) were estimated by minimizing the difference between the observed and predicted data. The resultant values are consistent with the specifications used in the manufacture of the sample. It may be possible to further improve the model accuracy by including effects such as the nonuniform illumination of the Cassegrain aperture (e.g., the supports for the secondary reflector obstruct a small portion of the aperture). Nevertheless, the results presented here indicate that the level of modeling proposed here can substantially help in understanding recorded data as well as optical effects in IR microspectroscopy.

SIMULATION AND PREDICTION

Instrumentation Effects. In simulation, it is possible to separate effects due to the sample and substrate and effects due to the instrumentation. Here, this is first accomplished to investigate the dependence of the measured spectra on the numerical aperture of the imaging system. Sample-induced distortions can result from changes in reflection and/or transmission coefficients between the background and sample measurements, an effect represented in the second term of eq 35. To eliminate these coefficient changes, one can consider a nondispersive, weakly absorbing sample. Here the imaginary part of the sample index, $k(\bar{v})$, is taken to be 1/100 of the imaginary part of the index of toluene, and the real part of the refractive index, $n(\bar{v})$, is taken to be 1. Note that this is not a physically realizable material, as causality requires that changes in the absorption must necessarily be associated with changes in the real part of the refractive index.[43] However, the minimal perturbations of the complex refractive index allow the isolation of instrument-induced changes in the data.

A 200 μm thick layer of the sample is taken to be in direct contact with a substrate of barium fluoride for transmission measurements and with a substrate of gold in transflection measurements. The background measurements are simulated with only the substrate present. The large sample thickness, paired with the weak absorption, results in absorbance data comparable to those expected from an ideal measurement of a 2 μm thickness of toluene. The indices of barium fluoride and gold are calculated using published coefficients[37,44] in a Sellmeier equation. It should be noted that in this article the Sellmeier equation for the real index of barium fluoride has been extended beyond the transmission window in order to allow a consistent comparison with transflection systems for low wavenumbers. Numerical apertures of 0.2, 0.5, and 0.9 (as in Figure 4) are simulated in both transmission and transflection geometries and the illuminating light is taken to be unpolarized. Note that for each NA the central obscuration produced by the Cassegrain is taken to have a radius covering 20% of the NA. The NA of 0.5 is similar to that available in commercial microspectroscopy systems, while the NAs of 0.9 and 0.2 provide greater and lesser comparisons.

An estimate of the absorbance is found by evaluating eq 35, and the results are displayed in Figure 8a. Note that the absorbance has been normalized by the path length (in micrometers). In this idealized example, a good agreement between the measured absorbance and the actual absorbance is expected. However, overestimation of the absorbance by an amount that increases with the numerical aperture is predicted. This apparent violation of Beer's law arises because of the increasing path length through the sample associated with higher-angle rays, a phenomenon predicted by Blout et al.[11] The procedure of Blout et al. accurately predicts the errors of Figure 8a; however, a more general correction procedure must account for a coupling between measurements, sample structure, and all angles of incidence, a set of phenomena explored further in the following simulations.

Sample-Induced Distortions. Next, consider a toluene sample (i.e., with the index illustrated in Figure 6) on barium fluoride for transmission measurements and on gold for transflection measurements. To investigate the effect of sample-induced distortions, measurements are simulated for a variety of sample thicknesses. The background measurements are taken by replacing the sample with a medium of the same thickness as the sample but with index of $n = 1.47$. These background measurements are designed to represent an optimistic case, where Fabry−Perot type fringing effects in the background cancel similar effects in the sample measurement, giving a relatively good match between $T_S(\bar{v})$ and $T_0(\bar{v})$ (see eq 35). Hence, experimentally observed data will contain additional fringes arising from purely optical effects. Various methods have been proposed for correction of fringes.[45] It must be noted, however, that explicitly accounting for physical effects is likely to be more accurate than signal processing methods alone, as was shown in Figure 7. The illuminating light is taken to be unpolarized, while the NA of the system is modeled as 0.5 (with a central NA of 0.1 obscured by the secondary Cassegrain reflector).

The simulation results are shown in Figure 8b. In the transmission experiments, the estimates of absorbance are reasonably accurate. In transflection, however, errors in peak position, peak height, and band shape are predicted in the absorption spectra. Such distortions have also been observed experimentally.[46] As a consequence of the dispersion quantified by the Kramers−Kronig relations,[43] strong absorption peaks are accompanied by sharp changes in the real refractive index (e.g., see Figure 6). This results in a significant difference between the coefficients $T_0(\bar{v})$ and $T_S(\bar{v})$ seen in eq 35 and leads to distortions. Furthermore, when the sample thickness is on the scale of the wavelength, reflected and transmitted components interfere, resulting in a complicated interplay of dispersion, sample geometry, and absorption. The differences in the predicted spectra with sample thickness stem from these phenomena.

(39) Hawranek, J. P.; Jones, R. N. *Spectrochim. Acta* **1976**, *32A*, 99−109.

(40) Hawranek, J. P.; Neelakantan, P.; Young, R. P.; Jones, R. N. *Spectrochim. Acta* **1976**, *32A*, 85−98.

(41) Tan, T. L.; Wong, D.; Lee, P.; Rawat, R. S.; Patran, A. *Appl. Spectrosc.* **2004**, *58*, 1288−1294.

(42) Tan, T. L.; Wong, D.; Lee, P.; Rawat, R. S.; Springham, S.; Patran, A. *Thin Solid Films* **2006**, *504*, 113−116.

(43) Toll, J. S. *Phys. Rev.* **1956**, *104*, 1760−1770.

(44) Ordal, M. A.; Long, L. L.; Bell, R. J.; Bell, S. E.; Bell, R. R.; Alexander, R. W., Jr.; Ward, C. A. *Appl. Opt.* **1983**, *22*, 1099−1120.

(45) Griffiths, P. R.; de Haseth, J. A. In *Fourier Transform Infrared Spectrometry*, 2nd ed.; Wiley-Interscience: Hoboken, NJ, 2007; Chapter 11.1.3, pp 253−255.

(46) Gunde, M. K.; Aleksandrov, B. *Appl. Spectrosc.* **1990**, *44*, 970−974.
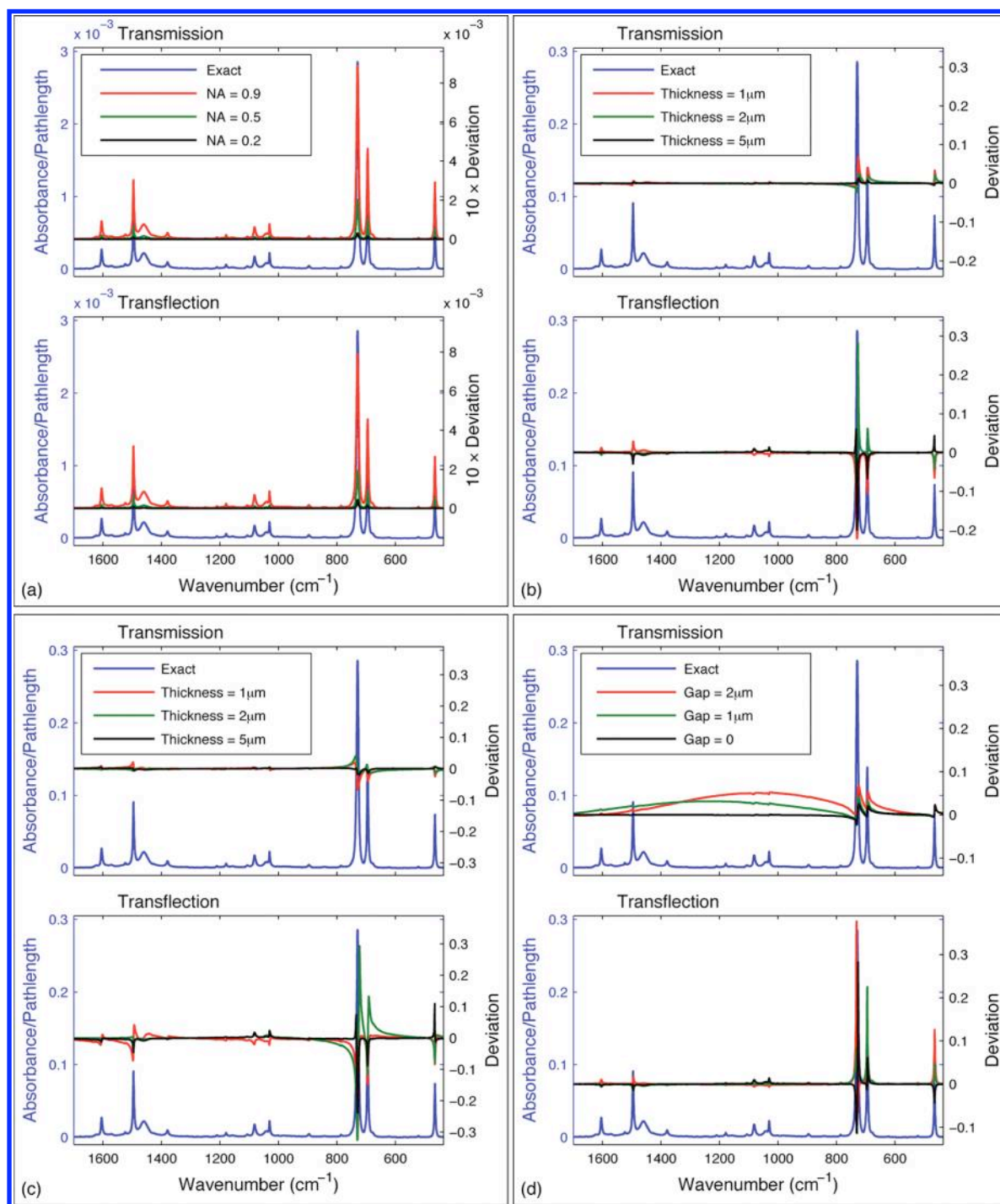
Figure 8. (a) Predicted absorbance for an idealized thick, low-absorption sample, normalized by the path length (in micrometers). Data are plotted for both transmission and transflection modalities (and for a range of numerical apertures) as differences from the ideal absorbance profile. In transmission, the substrate is barium fluoride, and in transflection, the substrate is gold. (b) Predicted path-length–normalized absorbance deviations for a toluene sample and a range of sample thicknesses. In transmission, the substrate is barium fluoride, and in transflection, the substrate is gold. (c) Predicted path-length–normalized absorbance deviations for a toluene sample and a range of sample thicknesses. In both transmission and transflection, the substrate is germanium. (d) Predicted path-length–normalized absorbance deviations when there is an air gap between the sample and the substrate. The air gap thickness is varied, while in all cases the sample thickness is 2 μm. In transmission, the substrate is barium fluoride, and in transflection, the substrate is gold. The absorbance spectra used to calculate the deviations shown here are plotted in the Supporting Information.

Sample-Induced Distortions for Substrates of Intermediate Index. The appearance of the dispersion profile (the real part of the refractive index) in absorption microspectroscopy measurements has been described.[13–15] It was noted that the estimate is more susceptible to this consequence of dispersion in transflection mode or when, for example, a higher-index substrate is used in

transmission. The dispersion influence can be explained, at least in part, by effects such as those predicted in Figure 8a. Romeo and Diem[13] also observed a similar feature at sample edges; this phenomenon is investigated in the follow-up article.[22]

If both the transmission and transflection substrates are germanium (with background measurements taken on the bare

germanium), the spectra predicted are shown in Figure 8c. The refractive index of germanium was calculated using published coefficients[36] for a Sellmeier model, and all other simulation parameters are the same as for Figure 8b. The germanium substrate can be seen to give seemingly confounding results; the transflection spectra have severe distortions including negative values of absorbance that are not physically realizable, while the transmission spectra have distorted band shapes and amplitudes. Hence, it is clear that the high index of germanium makes it unsuitable for accurate transmission or transflection measurements—without corrections for optical distortions. An ideal transmission substrate has an index matched to the sample, while an ideal transflection substrate is, for example, a strong conductor. At the toluene−germanium boundary both the transmission and reflection coefficients are significant and both are relatively sensitive to the sample index. As a result, the real part of the index is strongly coupled into the measurement. This coupling is particularly noticeable in the transflection measurement and results in apparently negative absorbance measurements. The transflection simulations of Figure 8b,c illustrate how the presented framework can be used to examine spectral distortions introduced in the transflection modality and suggests how explicit optical modeling may be useful in the design of transflection substrates.

Air-Gap-Induced Distortions. It is not uncommon in the mounting of a sample on the substrate to introduce a small air gap between the two; alternatively, the sample itself may contain a void. In Figure 8d, spectral distortions caused by such voids are shown for a variety of air gaps. The sample material is again toluene, and the background measurements are taken without accounting for the gap. Significant changes in peak shape, amplitude, and position can again be seen in transflection. The distortions are less severe in transmission although a significant nonzero baseline is observed. Findings consistent with these simulations have been reported with an underlying Matrigel layer and observed to depend on layer thickness[14] as seen here. However the effect was in that work attributed to a scattering effect based on a qualitative analysis. An alternative qualitative analysis attributes distortions to contributions from reflections from the top surface of a sample.[15] It was also reported by Romeo and Diem that poorly adhered or thin samples may produce a dispersive line shape,[13] consistent with results shown in Figure 8d. The rigorous model developed here accounts for both the observed results in a quantitative manner, as well as acting as a guide to understand potentially confounding effects in sample preparation. An understanding of this effect is especially relevant to cytological analyses in which single cells are analyzed for malignancy. Sample preparation becomes critical in those applications and has been reported to be a major challenge in developing IR microscopy for cytology.[47] The effect on tissue samples can be expected to be less drastic, as individual cell spectra are usually less important within the greater tissue structure, and both the spectral and spatial organization of the cells can be employed for effective diagnoses.[48]

Comparison with Bulk (Macro) Spectroscopy. The simulations presented above have shown how sample structure and the real (dispersive) part of the refractive index affect the recorded
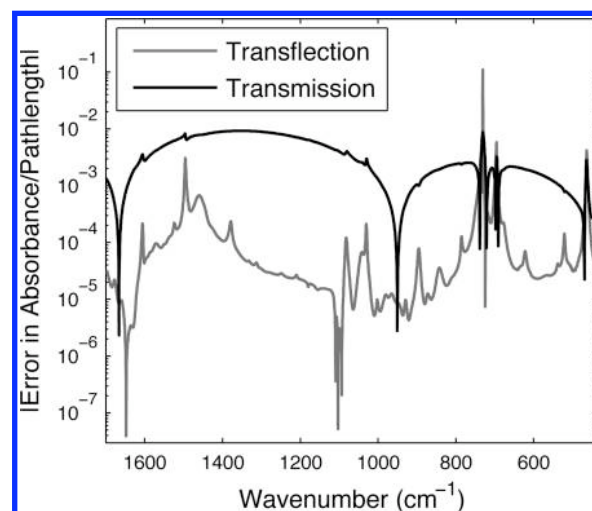

Figure 9. Magnitude of the difference between the data predicted in Figure 8d (for an air gap of 2 μm thickness) and the data predicted using a comparable single ray model.

spectral data. These effects produce apparent deviations from Beer's law if the simple model of eq 33 is applied. The importance of optical effects has been recognized for some time,[49−51] particularly in reflection-based modalities, and algorithms[38,52,53] have been developed to calculate the complex refractive index from certain types of data measured in bulk spectroscopy. In systems without tight focusing, this type of approach has been applied to correct for the apparent artifacts[21,39,40,54−59] and should be used where possible. In addition to general interference and dispersion effects (as observed without tight focusing in bulk-sample spectroscopy), the model developed in this work takes into account optical effects produced by the tightly focused illumination and collection of light. If focusing effects are negligible in comparison with the effects already modeled in bulk spectroscopy, it can be expected that existing correction algorithms will interpret microspectroscopy data correctly.

Figure 9 shows the difference between the focused-model, 2 μm-air-gap data of Figure 8d and those calculated for the same sample but using a single representative ray path (i.e., a model without focusing). For the transmission system, the representative ray path is taken to be at normal incidence, and for the transflection system, the median reflected path is chosen. The single-ray approach does not capture effects due to focused path length difference [as illustrated in Figure 8a] and, as seen in Figure 9, will not fully capture the behavior of the tightly focused system. For this example, the

(47) Romeo, M.; Mohlenhoff, B.; Diem, M. *Vib. Spectrosc.* **2006**, *42*, 9–14.
(48) Pounder, F. N.; Bhargava, R. Submitted for publication.

(49) Greenler, R. G. *J. Chem. Phys.* **1966**, *44*, 310–315.
(50) Greenler, R. G. *J. Chem. Phys.* **1969**, *50*, 1963–1968.
(51) Mendelsohn, R.; Brauner, J. W.; Gericke, A. *Annu. Rev. Phys. Chem.* **1995**, *46*, 305–334.
(52) Dienstfrey, A.; Greengard, L. *Inverse Probl.* **2001**, *17*, 1307–1320.
(53) De Sousa Meneses, D.; Rousseau, B.; Echegut, P.; Simon, P. *Appl. Spectrosc.* **2007**, *61*, 1390–1397.
(54) Andermann, G.; Caron, A.; Dows, D. A. *J. Opt. Soc. Am.* **1965**, *55*, 1210–1216.
(55) Hawranek, J. P.; Neelakantan, P.; Young, R. P.; Jones, R. N. *Spectrochim. Acta* **1976**, *32A*, 75–84.
(56) Bertie, J. E.; Apelblat, Y. *Appl. Spectrosc.* **1996**, *50*, 1039–1046.
(57) Yamamoto, K.; Ishida, H. *Vib. Spectrosc.* **1997**, *15*, 27–36.
(58) MacDonald, S. A.; Schardt, C. R.; Masiello, D. J.; Simmons, J. H. *J. Non-Cryst. Solids* **2000**, *275*, 72–82.
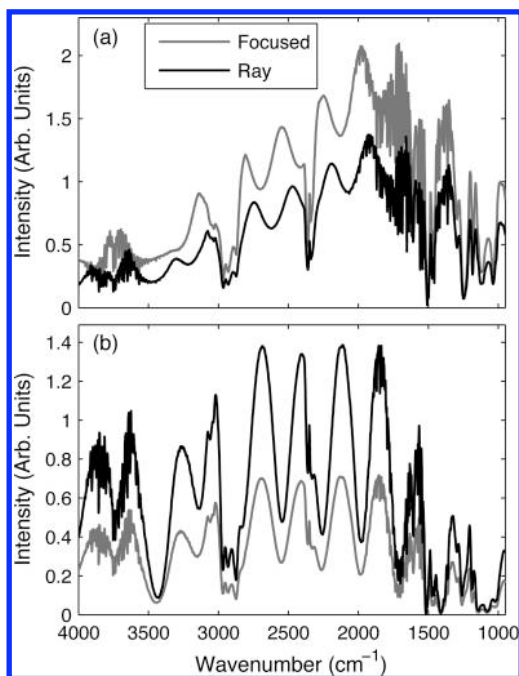(59) Moore, D. S.; McGrane, S. D.; Funk, D. J. *Appl. Spectrosc.* **2004**, *58*, 491–498.

Figure 10. Ray-based and fully focused predictions for (a) transmission and (b) transflection modalities and the experimental benchmarking sample.

single-ray simplification produces errors in the transflection system in particular. It is noteworthy that contemporary instruments can produce signals with low enough noise to observe absorbance values in the 10^{-1} to 10^{-4} range. Hence, these errors are significant, and the detailed model developed here should be used.

Differences between the focused and single-ray models arise from the angular dependence of the light−sample interaction. The difference between the full model spectrum and that predicted using a single ray model is shown in Figure 9. It is seen that this angular dependence can be significant, particularly around regions of high absorption. For the simpler samples considered in Figure 8b (i.e., air−sample−substrate systems with no air gap), the angular dependence is less critical and gives maximum path length-normalized absorbance errors of 0.0044 in transmission and 0.011 in transflection, as compared to maximum errors of 0.0046 and 0.11 in transmission and transflection, respectively, in Figure 9. Conversely, many-layer sample−substrate systems, with comparable transmission and reflection coefficients at layer boundaries, may be highly sensitive to incidence angle and hence to focusing effects. In Figure 10, a comparison between ray-based and focused models for the experimental benchmarking system (see Figure 7) is presented. For this more complicated sample−substrate system, the use of the ray-based model introduces significant errors. Focusing effects therefore play a very significant role when modeling the benchmarking sample used in the experimental validation of the model.

The analyses presented here should be used as a guide to estimate the precision in the data. The first implication is that the choice of sampling mode and/or substrate greatly influences the magnitude and form of systematic error introduced into the measurement. A second result demonstrates that there is a dramatic difference in the precision achievable by transmission mode and transflection mode microspectroscopy. The distortion is nonlinear and not trivial to correct. One practical implication is

that the noise in the data acquired must be no smaller than the observed deviation from the true spectrum. Any further reduction in noise would make the analytical conclusions limited by systematic distortions and not random noise. In general, the presented theoretical framework should be considered a starting point for detailed optical modeling in specific studies. In biomedical applications, where spectral assignments are challenging and spectral changes are small, detailed modeling can be expected to be important in understanding biochemical changes accurately.

CONCLUDING REMARKS

A mathematical model for mid-IR microspectroscopy has been derived by solving Maxwell's equations in layered media and for focused illumination and detection. Predictions given by this model are consistent with experimental results and with observations reported in the literature. It is seen that the interplay of focusing, the sample geometry, and strong dispersion fully accounts for the spectral response and apparent artifacts for simple homogeneous systems. Additional spectral effects that are produced by scattering within heterogeneous materials are addressed in part II of this work.

The model developed here can be applied to both transflection and transflection collection geometries. While transmission spectra demonstrated some robustness to distortions, transflection systems were seen to be particularly sensitive to focusing, dispersion, and sample−structure induced distortions. Ideally the distortions observed may be corrected by mathematically inverting the developed model, in order to estimate optical constants of the sample directly. However, in many cases of interest, the sample structure (i.e., the materials present in sample layers and the layer thicknesses) may not be known. This complicates the inversion process, as the sample geometry must be coestimated with the optical constants of the material of interest.

Spectral distortions due to sample structure (e.g., interference between interfaces) and dispersion have previously been reported for systems that do not employ tight focusing. The model presented here describes tightly focused fields throughout the sample and also predicts focusing dependent distortions that may impact the measured spectra for certain sample geometries. In comparison to typical experimental noise in modern IR microspectroscopy systems, the effects were found to be significant. Consequently, the model described provides a means to understand distortions that may limit the analytical capability of IR microspectroscopy.

SUPPORTING INFORMATION AVAILABLE

Additional information as noted in text. This material is available free of charge via the Internet at http://pubs.acs.org.